NURETH14-036

EXPERIMENTAL INVESTIGATION OF AIR BUBBLE FLOWS IN A WATER POOL

B. Balewski, S. Gupta, K. Fischer and G. Poss Becker Technologies GmbH, Eschborn, Germany

Abstract

This paper presents experimental results on rising bubbles in the wetwell of a boiling water reactor (BWR) in a loss-of-coolant accident in the pressure suppression pool (PSP). This accident scenario includes three processes: blowdown and associated water slug phenomena, bubble dynamics and related water flow during continuous release of gases and development of a thermal stratification. The paper covers the middle phase where air is fed through a downcomer. The developments of bubble formation and bubble flow are investigated by means of high speed videos. Diameter, velocity, formation frequency and breakup distance of bubbles are evaluated using automated image evaluation procedures. The experiments have been performed in the cylindrical vessel of the THAI test facility with a height of 9.2 m and a diameter of 3.2 m.

Introduction

The THAI (Thermal-hydraulics, Hydrogen, Aerosols and Iodine) experimental program investigates issues related to thermal-hydraulics, the transport of fission products like aerosols and iodine, the interaction with containment structures and passive safety systems [1]. The results of these experiments are used to validate Computational Fluid Dynamics (CFD) and Lumped Parameter (LP) codes [2, 3].

One of the actual research topics is the study of the bubble dynamics associated with the release of non-condensable gases via downcomer pipes to the wetwell pool. Such conditions can be expected during a severe accident when gases are released from the damaged core, pressurizing the drywell compartment. The radioactive fission products which are carried with these gases are partly retained in the water pool. In order to determine the efficiency of this pool-scrubbing effect, the bubble size spectrum and the bubble rise velocities must be known.

Pool scrubbing experimental investigations and model development have been conducted actively during 1985-1995 [4,5,6,7], resulting in the establishment of the codes SPARC, SUPRA and BUSCA for pool scrubbing simulation. The experimental basis of these codes is limited in several aspects, one of them being the detailed description of the bubble column development and the associated flow fields of water and gas. Progress in optical measurement technology and image processing methods was the motivation to relaunch an experimental investigation in these topics. The aim of this activity is to provide data for pool scrubbing model improvement, in particular to allow for a more accurate determination of the gas-water contact times during bubble column flow.

1. Experimental setup

During the processes of bubble formation at the downcomer exit and the subsequent bubble collapse, irregular objects of gas in water are formed. One way to quantitatively estimate these processes is an image based evaluation. To observe the progression of bubble columns in detail, especially the bubble dynamics near the exit of the downcomer pipe, a high speed camera is used. For using such a camera the most important and most challenging part is to install a light source which meets the following demands. First, a large area has to be illuminated to cover the whole process of bubble dynamics. Second, the light intensity has to be as high as possible to have enough light to ensure the high frame rates necessary to observe the development of the bubbles at sufficient temporal resolution as well as to reduce the exposure times of the camera to minimize motion blur. The third point is the requirement of a homogenous light distribution in a backlight configuration. This is needed to achieve shadow images that can be automatically evaluated by image processing explained later in the paper. The last important point is to place the light source as far as possible away from the bubble column to avoid any influence of the light source onto the bubble column. To fulfill all these requirements, two arrays of several waterproof neon lamps covered by two layers of thin Teflon® foil were installed in the water pool in a distance of 1 m from the downcomer. One array covers a region of approximately 1 by 0.6 m² near the downcomer exit. The other is placed near the water surface and covers a field of view of 0.12 by 0.7 m².

To further improve the image quality, a high performance high-speed camera (Photron FastCam SA1.1) was used which can record with full resolution of 1024 by 1024 Pixel at a frame rate of 5400 fps. This is more than the 1000 fps required here, but due to the very sensitive camera sensor the relative low light intensity is compensated and a relatively short exposure time of 18 µs is possible. A sketch of the experimental setup showing the test configuration and the camera positions is given in Figure 1.

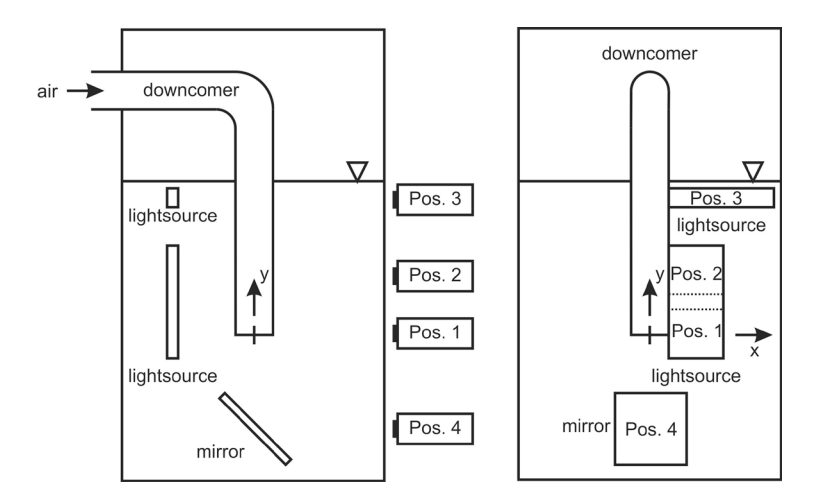


Figure 1 Front and side view of test facility with illumination and camera positions.

Images are taken at four different positions. Position 1 and 2 near the pipe exit and position 3 near the water surface are shadow images. Only one side of the pipe is observed which is sufficient due to the rotational symmetry of the bubble columns. This symmetry was confirmed by images taken from position 4 providing a view on the pipe exit from below.

Since this is not a real shadow image and due to an insufficient illumination no automatic evaluation is possible in this case. The image resolution is 0.65 mm/Pixel; only for position 3 the resolution is two times higher with 0.32 mm/Pixel since here only small bubbles are present.

The test setup represents one sector of a BWR wetwell water and gas space surrounding a single downcomer pipe corresponding to a 1:59 scale model the German Brunsbüttel plant wetwell with an original pipe diameter of 0.6 m. The downcomer pipe has a wall thickness of 5.6 mm and an inner diameter of 0.1 mm which was chosen to bring the mass flow into the same range as in the real downcomer. It is submerged 2 m into the pool and used to inject air at a temperature of 293 K with mass flow rates from 12 kg/h up to 110 kg/h. The pool has a width of 3.2 m and contains water at 286 K.

2. Image evaluation

The results presented in this paper are mainly based on automatic image evaluation. An automatic evaluation procedure is absolutely necessary for this kind of research to create a reliable data base which is based on a large amount of evaluated events. To provide such large data base by hand is beyond any reasonable effort, hence software for bubble evaluation is needed. The software to achieve this is an adapted and further improved version of software developed and approved for droplet and filament detection in spray applications [8]. The basic principle of the evaluation is to detect objects in black and white images analyzing their position, shape and area. For this purpose shadow images are required since only for this type of imaging the projected size of the objects is independent from the incident light and the position of the bubbles in the image.

The first step in this process is to subtract from an image with bubbles a background image without bubbles. The result is an image containing only the bubbles which one is interested in. In the next step a threshold value is defined to transform this image into a black and white or binary image. The threshold level is chosen in a way that the resulting black object corresponds as closely as possible to the area of the corresponding bubble. In order to find the right value, different threshold levels are tested. As a first check the original image and the binary image are manually compared. The second check is a sensitivity analysis of e.g. the mean bubble diameter distribution for different thresholds. In the present case we found that small variations in the threshold levels had nearly no effect upon the results. After the conversion into a binary image, all objects in the image are detected automatically. Their positions in x and y direction, the areas as well as the minor and major axes of the ellipsoidal projection are calculated. In addition an equivalent diameter corresponding to a circle with the same area as the area of the detected object is calculated. This procedure is done for three subsequent images with 5 ms time delay. This larger time step is taken since sometimes the velocities are so low, that a shift for an object of less than one Pixel in 1 ms is present. To be able to distinguish between real objects and e.g. dirt on the window the larger time step of 5 ms is chosen. By comparing positions and sizes of the objects in all three images, corresponding bubbles are identified. The advantage of this procedure is on the one hand an improved quality of the data due to the fact that only objects found in all three images are taken into account for all further evaluation steps. On the other hand additional information on the velocity in x and y direction are now available. To sum up, for each bubble detected in the

image area A, equivalent diameter d, major and minor axis l_1 and l_2 , position and velocities in x and y direction are provided.

All results from the automatic image evaluation presented here are based on the evaluation of 20000 images taken at four different points in time for each flow rate.

The limitation of the image based calculations is the limited image resolution. Table 1 gives an overview of the relevant restrictions and uncertainty in the calculated values. The minimum bubble diameter is simply defined by the resolution, the minimum velocity by a position change of one pixel divided by the time step of 5 ms between two subsequent images. The uncertainty in the volume of the initial ring bubble is mainly determined by the radius of the cross section since the volume is calculated using the square of the radius as shown later.

	Position 1, 2 and 4	Position 3
resolution [mm/Pixel]	0.65	0.32
minimum bubble diameter [mm]	0.73	0.36
minimum velocity [m/s]	0.13	0.06
uncertainty of ring bubble volume [%]	8	_

Table 1 Restriction and uncertainty of the image based evaluation.

3. Experimental results

In all experiments, qualitatively the same bubble dynamics are observed. At the end of the downcomer a ring bubble is formed. At the beginning the ring bubble expands a few millimeters downwards and then starts to expand in upward direction. After a certain time the ring bubble detaches from the pipe exit and starts to ascend along the pipe wall. The cross section of this torus-like ring bubble is approximately elliptically shaped with the minor axis located in the horizontal direction. Due to hydrodynamic instabilities this ring bubble starts to deform and subsequently breaks up into smaller bubbles. For a very short time period of a few milliseconds, larger and relatively irregular formed bubbles are present which then also disintegrate into smaller bubbles with a diameter less than approximately 20 mm. This process is shown in Figure 2 by images taken at a mass flow rate of 40 kg/h, and it is illustrated schematically in Figure 3.

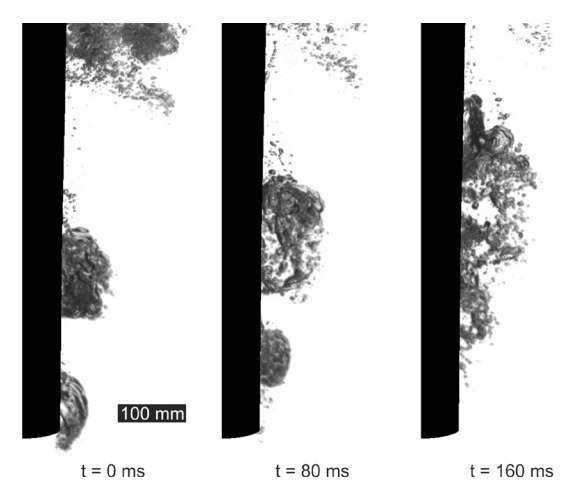


Figure 2 High-speed images near the pipe exit at three different points in time.

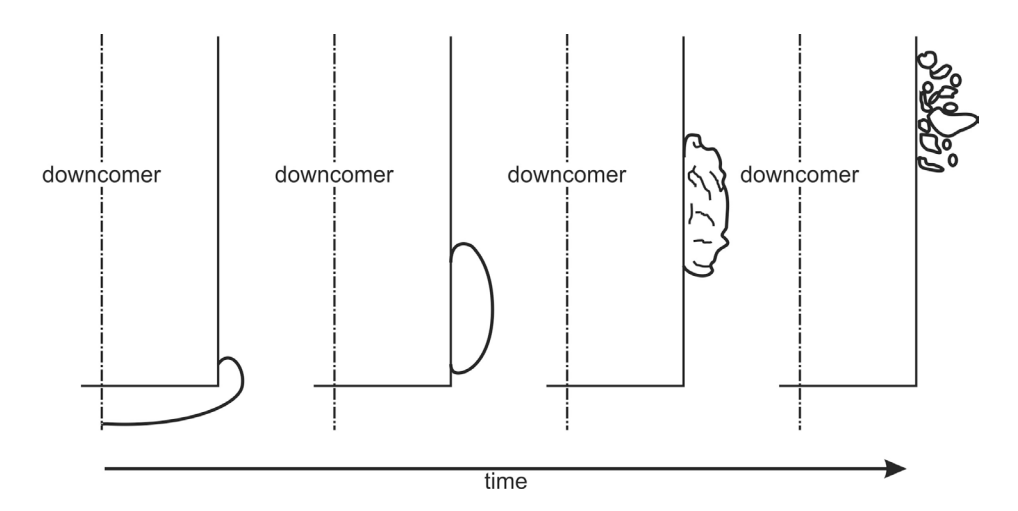


Figure 3 Schematical illustration of ring bubble formation and disintegration of ring bubble into smaller bubbles.

Further up the breakup of large bubbles continues until the bubble diameter reaches a final size in the order of 4 mm (Fig. 4). Simultaneously, the bubble column radially spreads more and more starting from a very high bubble density in the region of the ring bubble breakup until a moderate bubble density close to the water surface. The bubble density near the downcomer pipe wall is always higher compared to regions radially farther away. Due to the fact that the small bubbles are formed from ring bubbles produced at a certain frequency, also the bubble density in this region near the surface varies over time. The bubble distribution spreads in vertical direction to partly fill the gaps from the ring bubble creation intervals.

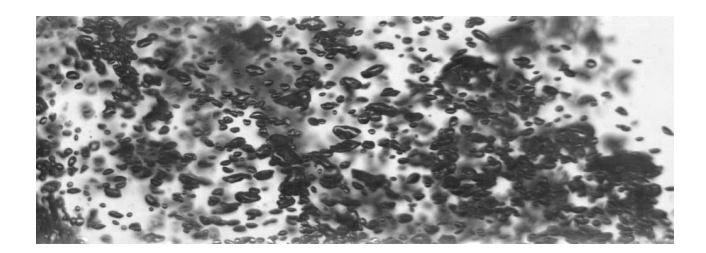


Figure 4 High-speed image of bubbles near the water surface. The field of view is 110 by 320 mm² with the downcomer pipe located at the left. Mean bubble diameter is 4 mm.

3.1 Ring bubble formation

The formation frequency of ring bubbles is evaluated first. This allows to estimate the ring bubble volume from the mass flow rate.

For all cases investigated here, a constant formation frequency of approximately 4 Hz was found by two different methods. The first is the evaluation by hand based on the images of the pipe exit from Position 4 and the side view at Position 1. Keeping the effort on a reasonable level, this was done for 20 ring bubbles per flow rate. The scattering of the results was low. In addition, by evaluating the camera view from below (Pos. 4) it was confirmed that for all flow

rates the formation of a ring bubble is observed. Except for the lowest mass flow rate of 12 kg/h a closed ring cannot be observed in any case.

The second method to estimate the formation frequency is to use the results from the automatic image analyses in combination with a frequency analyses. For this purpose, the number of bubbles with their lowest point 5 mm above the pipe exit is recorded over time. For all flow rates a clear peak around 4 Hz appears. An overview of found frequencies is given in Table 2 together with the standard deviation which is nearly the same for all cases and independent of the evaluation method.

mass flow rate [kg/h]	12	24	40	80	110
evaluation by hand [Hz]	4.1	3.9	4.3	4.2	4.4
automatic evaluation [Hz]	3.9	4.4	4.3	3.8	4.2
standard deviation [Hz]	1.0	1.0	1.0	1.1	1.2

Table 2 Ring bubble formation frequency at different mass flow rates.

Combining all results a mean formation frequency of 4.1 Hz is found. This can be compared with results in [9] where two mean formation frequencies of 2.8 Hz and 1.3 Hz for downcomer pipe diameters of 0.15 m and 0.6 m are found.

Including the present result of f = 4 Hz with a downcomer pipe diameter of D = 0.1 m, the variation of the ring bubble formation frequency with the downcomer diameter can approximately be correlated as

$$f = 0.1 \cdot \sqrt[3]{\frac{\sigma \cdot g}{\eta \cdot D^2}} \tag{1}$$

where g is the gravitational acceleration, σ the surface tension and η the dynamics viscosity of the water. This correlation and the frequencies are plotted together in Figure 5.

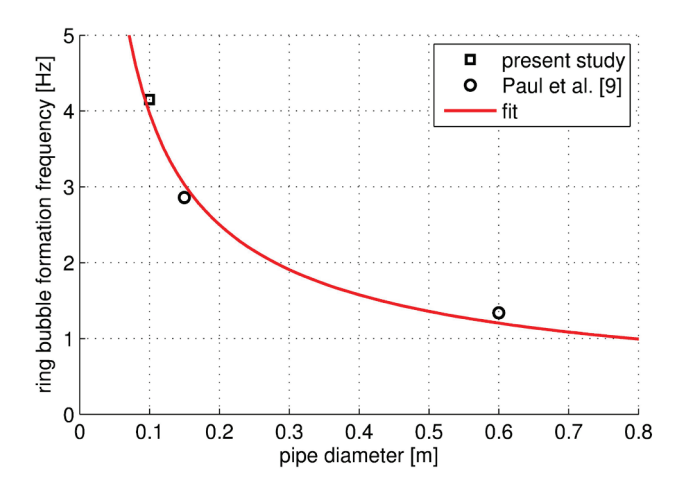


Figure 5 Ring bubble formation frequencies for different downcomer pipe diameters.

3.2 Ring bubble size

The size of the ring bubble is also calculated based on two different methods. The first is again the evaluation of the bubble dimension in the images by hand at camera position 4. The second is based on the size of bubbles which have just detached from the pipe exit.

To calculate the real volume of the ring bubble, the volume is estimated by a torus with a circular cross section as shown in Figure 6 as

$$V_{torus} = 2 \cdot \pi^2 \cdot R \cdot r^2 \tag{2}$$

where R is the radius of the torus and r is the radius of the cross section. Hence in both cases the volume cannot be calculated directly. The automatic calculation provides information about the cross section of the torus-like equivalent diameter, major and minor axis of the surrounding ellipse and the center of mass. The radius r of the cross section is now defined by the equivalent diameter and the radius R is the distance in x-direction of the center of mass to the center of the pipe. In order to crosscheck this automatic calculation, an evaluation by hand was performed, giving the outer diameter of the torus d as it is illustrated in Figure 6. Thus the radius r is calculated by using the downcomer diameter D as

$$r = \frac{1}{4} \cdot (d - D) \tag{3}$$

and the radius R as

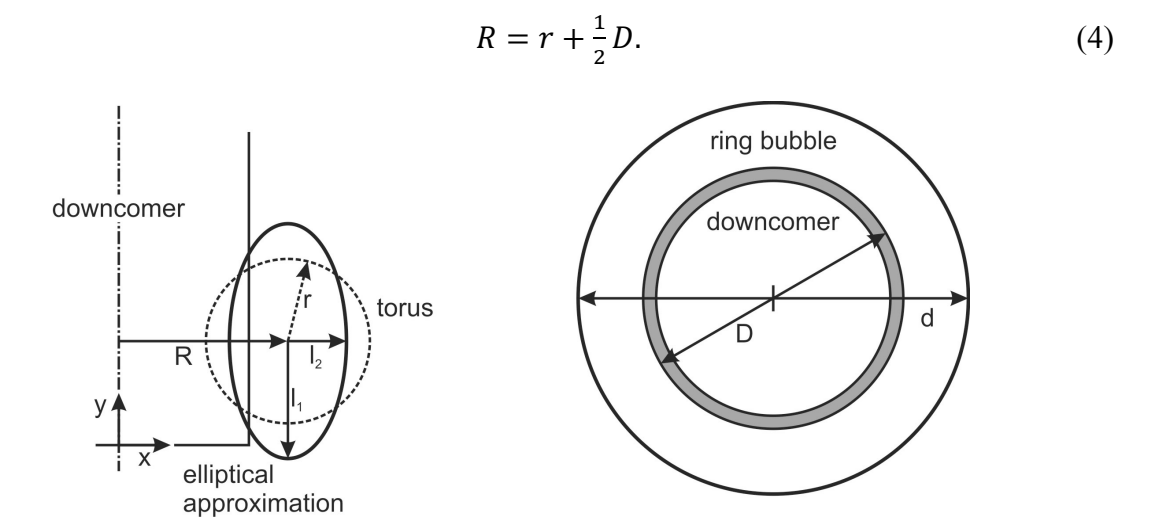


Figure 6 Sketch of the downcomer together with the torus geometry with different approximations. Side view on the left; view from below on the right.

In Figure 7 both results are plotted together with the expected volume based on the corresponding injection mass flow rate and assuming a constant formation frequency of 4 Hz. The red curve for the automatic evaluation fits very well whereas the blue curve of the hand evaluation is significantly lower compared to the expected values. This is due to the fact that the view from below shows only the dimension of the ring bubble in x-direction. From the

side view onto the pipe exit it is obvious that the ring bubble has larger dimensions in y-direction. Thus the volume of the ring bubble is underestimated. To compensate this, the ratio of minor l_2 and major l_1 axis are taken from the automatic evaluation to adjust the radius of the cross section using the equation

$$r' = r \cdot \sqrt{\frac{l_2}{l_1}}. (5)$$

The ratio $\frac{l_2}{l_1}$ is approximately 2.1 and independent of the flow rate. With this modification, the calculated volume fits better, as can be seen from the green curve in Figure 7. The spread between the curves is caused by the asymmetry of the ring bubbles which are not completely closed.

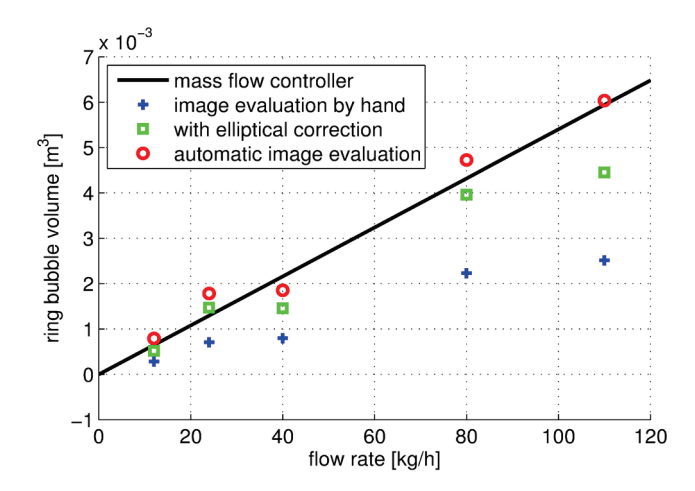


Figure 7 Ring bubble volume versus flow rate evaluated with different methods.

3.3 Breakup length

The next interesting point is the distance relative to the pipe exit where the ring bubble disintegrates into smaller bubbles. Since this is a very chaotic process it is not easy to determine this point. As seen in Figure 2 the ring bubble close to the pipe exit is nearly transparent indicating a relatively smooth surface. Rising higher the surface gets disturbed, leading to a nearly opaque bubble. After this stage the bubble rapidly breaks up into smaller ones. In this work the breakup length is defined as the vertical distance from the downcomer exit where the initial bubble just started to disintegrate.

To identify this location, the bubble diameters along the y-direction averaged in x-direction are calculated resulting in a profile providing the bubble diameter along the vertical axis. The result can be seen in Figure 8.

The curves show the presence of large bubbles in the lower region, small bubbles in the upper region, and a sudden transition between the two regions. In the large-bubble region, the diameter increases with the flow rate. In the small-bubble region, the diameters are nearly independent of the flow rate. Only for the lowest mass flow rate of 12 kg/h the transition is

smoother. The explanation for the sudden transition is the fact that the software is not able to detect a large bubble any more since this bubble decays into smaller bubbles within less than 20 mm rising distance. This breakup does not occur via disintegration into few larger globules which then subsequently further disintegrate, as described in [9]. Instead it is more like a fast break up into a large number of smaller nearly spherical bubbles and a small number of larger bubbles with a very irregular shape. The latter exist only a few milliseconds before they also collapse into smaller bubbles. In contrast to this rapid process, the breakup at lower flow rates is based on a slower and less chaotic disintegration of the ring bubble. Especially in the case of 12 kg/h mass flow rate, no closed ring is formed at any time; in this case the breakup of large globules is the starting point of the disintegration process. This breakup is less violent resulting in a smoother decrease of the mean bubble diameter during bubble rise.

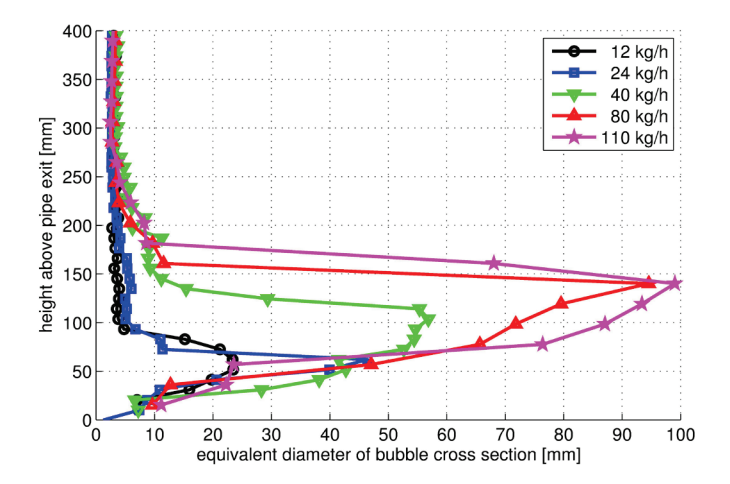


Figure 8 Average bubble diameter of detected bubbles along the downcomer axis.

Assuming the bubble disintegration starts from a large bubble (not necessary a closed ring bubble) the maximum value of the equivalent diameter just before the breakup is taken as an initial diameter d_i. According to [9] an normalized initial bubble volume

$$C_N = \frac{2}{3} \cdot \frac{d_i^3}{D^2} \cdot \sqrt{\frac{\rho \cdot g}{\sigma}} \tag{6}$$

can be plotted over the injector Weber number

$$We = \frac{u^2 \cdot \rho \cdot D}{\sigma} \tag{7}$$

where u is the mean injection velocity of the air. The results together with these from [9] are shown in Figure 9. It can be seen that all points fit well to the model used in SPRAC [6] which calculates the initial volume according to

$$C_N = 0.0891 \cdot \text{We}^{0.616}$$
 (8)

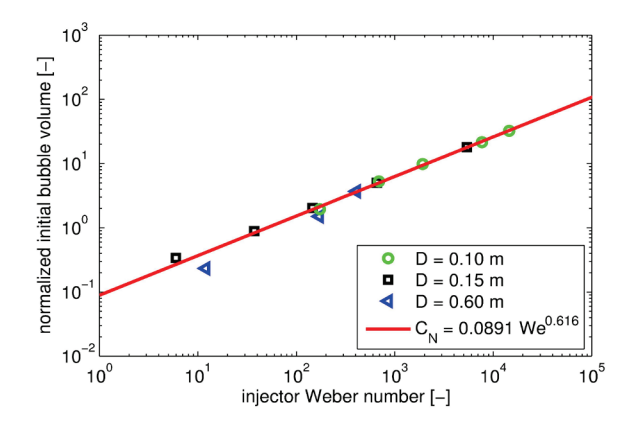


Figure 9 Normalized initial bubble volume versus injector Weber number.

3.4 Bubble diameter near the pool surface

Near the pool surface the bubble column consists of small bubbles. The distribution of bubble diameters near the surface is plotted in Figure 10. The diameter of the bubbles in this region is in the range of 3 to 4 mm, independent of the mass flow rate and the radial position. As expected the maximum radial position until which bubbles can be detected increases with the flow rate. Close to the downcomer, for the higher flow rates no data are available as the bubble density is too high for automatic evaluation. To overcome this difficulty, a particle size analyzer from Carl Zeiss TGZ 3 [10] was used to manually evaluate bubble sizes in these dense regions, which leads to the same size range as found before. In this case the statistical samples are substantially smaller than those obtained by the automatic evaluation, where approximately 20000 bubbles were found in the observed region, but combined with the cross check by human eye these results can be considered as reliable.

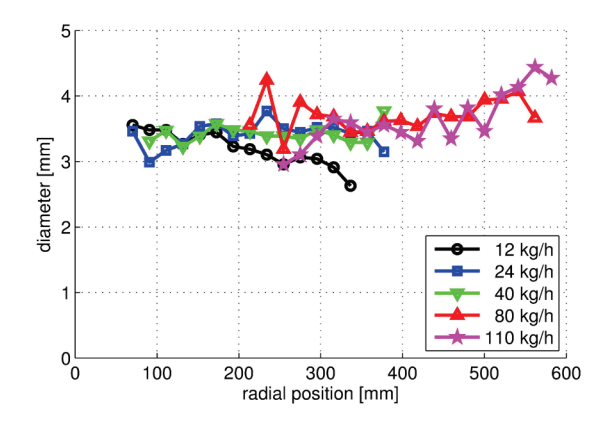


Figure 10 Bubble diameter close to the water surface 1900 mm above the downcomer exit.

3.5 Rising velocity

The image evaluation also provides the rising velocity of the bubbles and at various radial locations. In Figure 11 the rising velocities of the bubbles are plotted at different elevations.

Up to the height of 0.75 m the distributions for the different flow rates are close together, and only in the region near the surface a clear spreading is observable with higher velocities for higher flow rates due to entrainment of ambient liquid into the bubbly region.

The radial velocities are in the order of 0.1 to 0.2 m/s independent of flow rate and position.

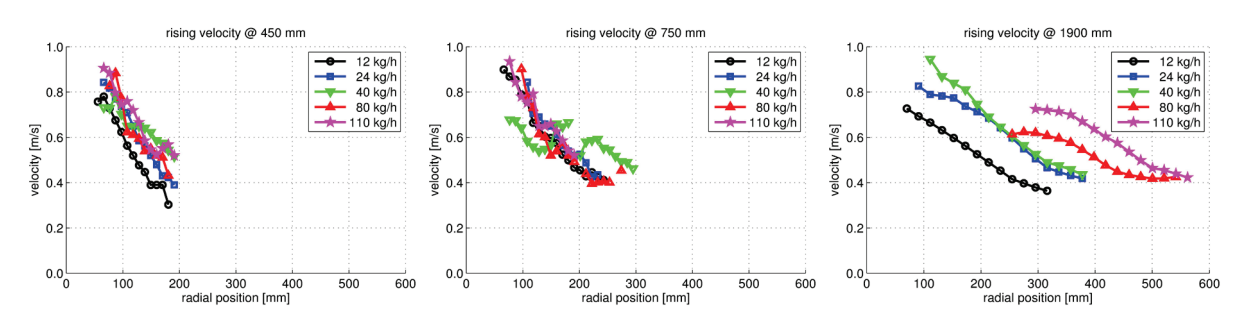


Figure 11 Rising velocities of bubbles at different heights.

3.6 Bubble column width

The width of the bubble column along the height of the pool is given in Figure 12 as an estimation out of long exposure images based on a decrease in the intensity ratio I/I_0 of the grayscale images with (I) and without bubbles (I_0). The threshold for the boundary is defined as the decrease of the intensity ratio down to two percent. This definition is chosen since other methods like the full width half maximum (FWHM) criterion are not suitable for the present bubble columns: near the downcomer pipe a relatively dense region is located with an abrupt decrease in direction away from the pipe. In contrast near the surface the decrease of the bubble density and therefore the intensity ratio is very smooth.

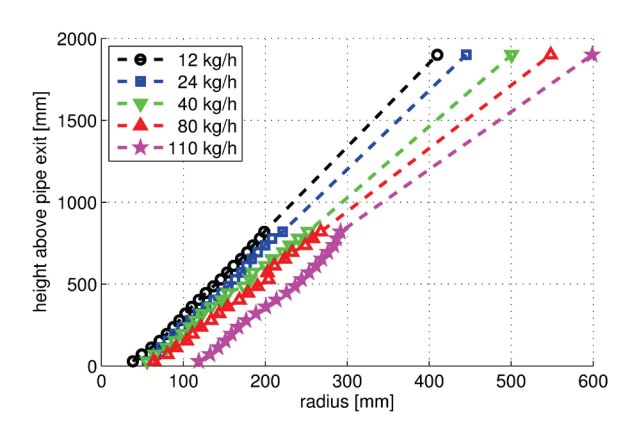


Figure 12 Width of bubble column at different mass flow rates.

4. Summary and Conclusion

This paper presents experimental investigations of bubble dynamics in the THAI test facility related to the suppression pool hydrodynamics for further development of LP and CFD codes. The bubble dynamics beginning with the formation of ring bubbles at the downcomer exit, the disintegration into smaller bubbles and the formation of a homogenous bubble cloud near the

water surface are observed using a high-speed camera. Based on these images initial diameters, formation frequency, breakup distance, bubble diameters and velocity distributions are determined. A correlation between formation frequency of the initial ring bubble and the initial downcomer pipe diameter was found and the use of the SPARC model for the initial bubble diameter just before the breakup into smaller bubbles was confirmed for a larger range of injector Weber numbers.

The next steps are now to evaluate the influence of different steam-air mixtures injected into to pressure suppression pool at different water temperatures.

5. Acknowledgments

This work is carried out in the frame of a research project funded by the German Federal Ministry of Economics and Technology, project number 150 1361. The authors would like to thank Prof. Cameron Tropea from the Technische Universität of Darmstadt for providing the high-speed camera.

6. References

- [1] S. Gupta, T. Kanzleiter, K. Fischer, G. Poss, "Reactor safety research program at THAI test facility", <u>17th Pacific Basin Nuclear Conference Cancún</u>, Q.R. México (2010).
- [2] H.-J. Allelein, K. Fischer, J. Vendel, J. Malet, E. Studer, S. Schwarz, M. Houkema, H. Paillère, A. Bentaib, "International standard problem ISP-47 on containment thermal-hydraulics", Report NEA/CSNI/R (2007)10.
- [3] S. Schwarz, K. Fischer, A. Bentaib, J. Burkhardt, J.-J. Lee, J. Duspiva, D. Visser, P. Royl, J. Kim, P. Kostka, R. Liang, "Benchmark on hydrogen distribution in a containment based on the OECD-NEA THAI HM-2 experiment", <u>NURETH-13</u>, Kanazawa, Japan, (2009).
- [4] K. Fischer, M.R. Kuhlmann, V. Kogan, "Fission product pool scrubbing data and modeling assessment", Report ACEX TR-A-01, December 1996.
- [5] M. Escudero Berzal, M.J. Marcos Crespo, M. Swiderska-Kolwalczyk, M. Martin Espigares, J. López Jiménez, "State-of-the-Art Review on Fission Product Aerosol Pool Scrubbing under Severe Accident Conditions", Report CIEMAT ITN/TS-22/DP-93, April 1994
- [6] P.C. Owczarski, K.W. Burk, "SPARC-90: A Code for Calculating Fission Product Capture in Suppression Pools", Report NUREG/CR-5765, PNL-7723 R1, October 1991
- [7] S.A. Ramsdale, "BUSCA-JUN 90 Reference Manual", Report AEA Technology, SRD R542, March 1991
- [8] B. Balewski, "Experimental investigation of the influence of nozzle-flow properties on the primary spray breakup", PhD thesis, TU-Darmstadt, Germany, 2009.
- [9] D.D. Paul et al., "Radionuclide scrubbing in water pools. Volume 2: Gas-liquid hydrodynamics with full-scale downcomers and horizontal vents", Report EPRI NP-4154-L, Volume 2, October 1991
- [10] F. Endter and H. Gebauer, Optik 13, pp. 97-101, 1956